Hindawi Publishing Corporation
International Journal of Photoenergy
Volume 2014, Article ID 391270, 7 pages
http://dx.doi.org/10.1155/2014/391270

Research Article

Thermal Field Analysis and Simulation of an Infrared Belt Furnace Used for Solar Cells

Bai Lu, Liang Zongcun, and Shen Hui

School of Physics and Engineering, Institute for Solar Energy Systems, State Key Laboratory of Optoelectronic Materials and Technologies, Sun Yat-sen University, Guangzhou 510275, China

Correspondence should be addressed to Liang Zongcun; 2713604996@qq.com and Shen Hui; 2323292429@qq.com

Received 29 January 2014; Accepted 7 April 2014; Published 12 May 2014

Academic Editor: Prakash Basnyat

During solar cell firing, volatile organic compounds (VOC) and a small number of metal particles were removed using the gas flow. When the gas flow was disturbed by the thermal field of infrared belt furnace and structure, the metal particles in the discharging gas flow randomly adhered to the surface of solar cell, possibly causing contamination. Meanwhile, the gas flow also affected the thermal uniformity of the solar cell. In this paper, the heating mechanism of the solar cell caused by radiation, convection, and conduction during firing was analyzed. Afterward, four 2-dimensional (2D) models of the furnace were proposed. The transient thermal fields with different gas inlets, outlets, and internal structures were simulated. The thermal fields and the temperature of the solar cell could remain stable and uniform when the gas outlets were installed at the ends and in the middle of the furnace, with the gas inlets being distributed evenly. To verify the results, we produced four types of furnaces according to the four simulated results. The experimental results indicated that the thermal distribution of the furnace and the characteristics of the solar cells were consistent with the simulation. These experiments improved the efficiency of the solar cells while optimizing the solar cell manufacturing equipment.

1. Introduction

Firing is an important step during the fabrication of crystalline silicon solar cell that affects the series-parallel resistance and the fill factor of the solar cells, determining the efficiency of the solar cells [1]. To form the front and back side contacts, metallization paste was printed on the silicon wafers using thick film technology and screen printing. A paste containing aluminum was used for the back side contact; silver was used for the front side contact fingers. Afterward, the pastes were fired in an infrared belt furnace. In the firing zone, the VOC and a few metal particles were removed by the gas flow. When the gas flow was disturbed by the thermal field of the furnace and structure, the metal particles in the discharging gas flow might randomly adhere to the surface of solar cell, causing contamination. Meanwhile, the gas flow also affected the temperature uniformity of the solar cell, causing stress concentration or breakage. Hoornstra et al. showed that the thermal field of the furnace was difficult to measure explicitly [2], making it a key issue.

When comparing the infrared belt furnaces with rapid thermal processing (RTP), they are similar during rapid heating. Cooper et al. [3] simulated RTP to study the physics of solar cell contact formation during mass production using a high-throughput infrared belt furnace. A lower Ag finger contact resistance was observed as the sinter dwell time decreased. Campbell et al. [4] calculated the steady-state temperature distribution and gas flow patterns in a RTP system under various process conditions. The gas flow patterns and temperature distributions were strongly dependent on the pressure and ambient composition. Kakoschke et al. [5] showed a theory of wafer heating during RTP and demonstrated that temperature uniformity was not only limited by radiation loss at the wafer edge in the stationary state, but was also influenced by transient effects during temperature ramping. Gyurcsik et al. [6] used the first-principles approach to model the RTP system for temperature uniformity. No uniform temperatures in the wafers in a RTP system could be counteracted by adjusting the relative power of the individual lamps used to alter the heat flux density at the wafer. However,

the firing furnace is longer, the solar cell is in motion, and the gas flow is heavy, and currently, no comprehensive studies are available.

In this paper, the heating mechanism for solar cells via radiation convection and conduction during firing was analyzed. Furthermore, four 2D models of the furnace were proposed and the transient thermal fields with different gas inlets, outlets, and internal structures were simulated. To verify the result, four types of furnaces were produced according to four simulated structures. The temperature distribution of the furnace firing and the characteristics of solar cell fired will be discussed in this study.

2. Heat Transfer Analysis

The heat transfer mechanism is shown in Figure 1; the near-infrared radiation is emitted from the upper lamps and lower lamps. Most of the radiation is absorbed by the solar cells and the furnace wall, while a small part is reflected and removed by the gas flow. Therefore, heat conduction occurs in the solar cell and the walls of the furnace. Meanwhile, convection occurs among the solar cells, the walls of the furnace and the gas flow. Therefore, the thermal field includes conduction, convection, and radiation.

2.1. Radiant Energy of Solar Cell from the Lamps. Figure 2 shows that a lamp is irradiating a solar cell, where AB denotes a linear light source of the near infrared. I_0 is the radiation intensity along the normal direction of the lamp. L is the radiance [W/(m^2·sr)]. l is the length of the lamp [m]. R is the radius of the lamp[m]. X is a point on the solar cell. h is the vertical distance from point X to the lamp [m], α_1 is the angle between $AX$and XC [°], and α_2 is the angle between BX and XC [°].

The maximum radiation intensity of per unit length is

$$I_l = \frac{I_0}{l} = 2LR. \tag{1}$$

The radiation intensity of dx in the DX direction is

$$dI_\alpha = I_l dx \cos\alpha. \tag{2}$$

The irradiance of dx at point X is

$$dE_\alpha = \frac{dI_\alpha}{r^2}\cos\alpha. \tag{3}$$

Figure 2 shows the following:

$$r = \frac{h}{\cos\alpha}, \qquad x = h\tan\alpha, \qquad dx = \frac{hd\alpha}{(\cos\alpha)^2}. \tag{4}$$

Therefore, the irradiance of dx at point X is as follows:

$$dE_\alpha = I_l\frac{1}{h}(\cos\alpha)^2 d\alpha. \tag{5}$$

The irradiance of AB at point X is as follows:

$$\begin{aligned} E_X &= \int dE_\alpha = I_l\frac{1}{h}\int_{\alpha_2}^{\alpha_1}(\cos\alpha)^2 d\alpha \\ &= I_l\frac{1}{h}\frac{1}{4}\left[2\left|\alpha_1-\alpha_2\right| + \left|\sin 2\alpha_1 - \sin 2\alpha_2\right|\right]. \end{aligned} \tag{6}$$

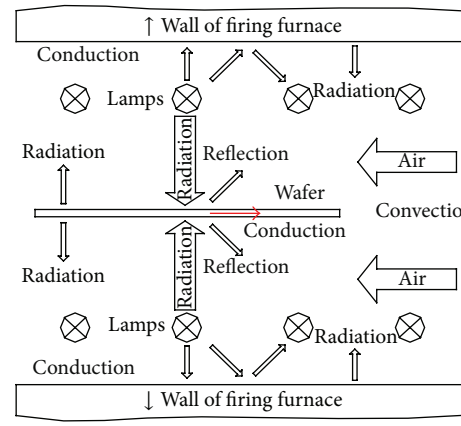

Figure 1: Heat transfer mechanism.

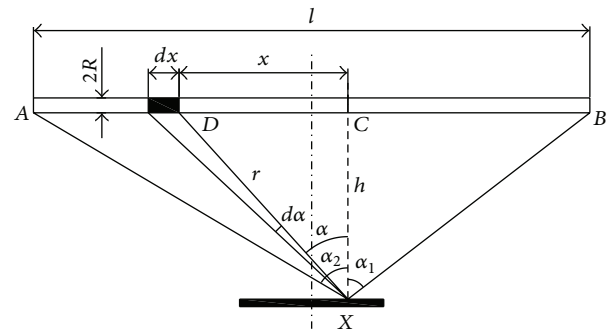

Figure 2: Irradiance of solar cell from lamp.

The radiant energy of a solar cell from AB is as follows:

$$Q_l = \iint E_x dA\, dt. \tag{7}$$

2.2. Radiant Energy of Solar Cell from the Walls. The radiant energy of solar cell from the wall is shown in Figure 3, where ΔA_s is a radiant source on the wall [m^2]. L is the radiance [W/(m^2·sr)]. ΔA is a small area irradiated on the solar cell [m^2]. j is the distance between ΔA_s and ΔA. θ_s and θ are the angles associated with n and j [°], respectively.

The radiation intensity of ΔA_s in the j direction is as follows:

$$I = L\cos\theta_S \Delta A_S. \tag{8}$$

The irradiance of ΔA is

$$E_w = \frac{I\cos\theta}{j^2} = L\Delta A_S\frac{\cos\theta\cos\theta_S}{j^2}. \tag{9}$$

The radiant energy of the solar cell from the wall is as follows:

$$Q_W = \iint E_w dA\, dt. \tag{10}$$

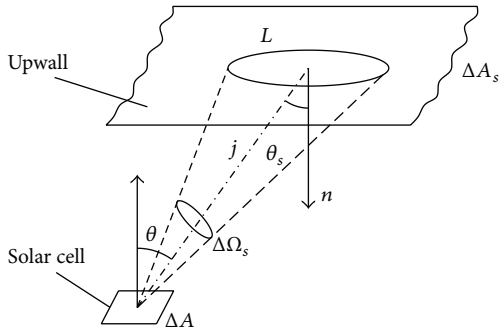

Figure 3: Irradiance of a solar cell from the wall.

2.3. Conduction Heat in the Solar Cell. The heat transferred via conduction in the solar cell could be expressed by Fourier's law

$$Q_\lambda = -\lambda A \frac{\partial T}{\partial n}, \tag{11}$$

where Q_λ is the conduction heat per unit time [w], λ is the thermal conductivity coefficient [W/(m·°C)], A is a surface area [m^2], and $\partial T/\partial n$ is the temperature gradient of solar cells [°C/m].

2.4. Convection Heat on the Solar Cell. Convection was a mixture of conduction and the motion of a fluid. As the gas flowed against the surface of the solar cell, heat was transferred via convection:

$$Q_\beta = \beta A \left(T_w - T_f\right), \tag{12}$$

where Q_β is the convection heat per unit time [w], β is the heat transfer coefficient [W/(m^2 °C)], A is a surface area [m^2], T_w is the surface temperature of solar cell [°C], and T_f is temperature of the gas [°C].

2.5. Total Energy. Based on the solution of (7), (10), and (12), the total energy of a solar cell from a lamp, ΔA_s and the convection is given by

$$Q = Q_l + Q_W + Q_\beta. \tag{13}$$

Eighty-four infrared lamps were present in the furnace, the internal surface of the furnace was large, and several ten solar cells were heated at the same time. Therefore, it was quite difficult to calculate the energy of all of the points on each solar cell according to the above formulas, and numerous computations were required. Thus, the numerical method was used to solve this problem in the paper.

3. Numerical Simulations

FLUENT is software for computational fluid dynamics (CFD). It employs a control-volume-based technique to convert the governing equations into algebraic equations that are solved sequentially using the implicit method [7]. In the paper, a first-order upwind scheme was used for the spatial dissociation of the convective terms; the SIMPLE algorithm was used to couple the pressure and velocity and solve the pressure-correction implicitly.

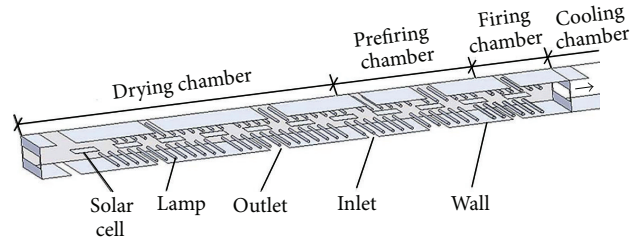

Figure 4: Sketch of firing furnace.

3.1. Physical Assumptions. When using FLUENT, some physical assumptions and geometric simplifications were employed. The radiant intensity of the lamps was assumed independent of direction, remaining constant across the length of the lamp and uniform at the cell lower surface. The cell was assumed to be infinitely thin. The temperature on the top surface of the cell was identical to the temperature on the lower surface. The chamber was axially symmetrical. The gas was incompressible and could be regarded as an ideal gas. All surfaces were defined as diffuse reflectors and emitters.

3.2. Geometrical Model. Figure 4 shows a sketch of the furnace. The furnace is of 6 m long and 0.16 m high, including a drying chamber, a prefiring chamber, a firing chamber, and a cooling chamber. Each chamber contains several walls, infrared lamps, thermocouples, mesh belts, inlets, and outlets. The infrared lamps are arranged on the top and the bottom inside the chambers symmetrically. Because many supports are added to make no contact between the solar cell and the mesh belts, the mesh belts are ignored in the modeling. The inlets and outlets in the chambers wall are used to remove the VOC that came from the paste.

If the 3D solid model of the furnace was used for simulation, the storage and calculation of data during the reconstruction process would be so enormous as to preclude calculation using common computers. Wacher [8] reported that a model of the radioactive heat transfer could occur in an axially symmetric RTP chamber, and a flow included in the RTP process could further improve the temperature uniformity. Therefore, simple and effective 2D models were used.

Based on the work above, four furnaces were proposed for studying the effect of inlets and outlets at different positions on the thermal field and the temperament of the solar cell surface. The four models are shown in Figure 5.

Figure 5(a) shows that all the gas inlets were in the upper portion, while outlets were in the lower portion. The gas flow distance was short, facilitating laminar flow formation and rapid VOC removal.

Figure 5(b) shows that each chamber had one pair of inlets and outlets. The VOC in each chamber were blown out independently.

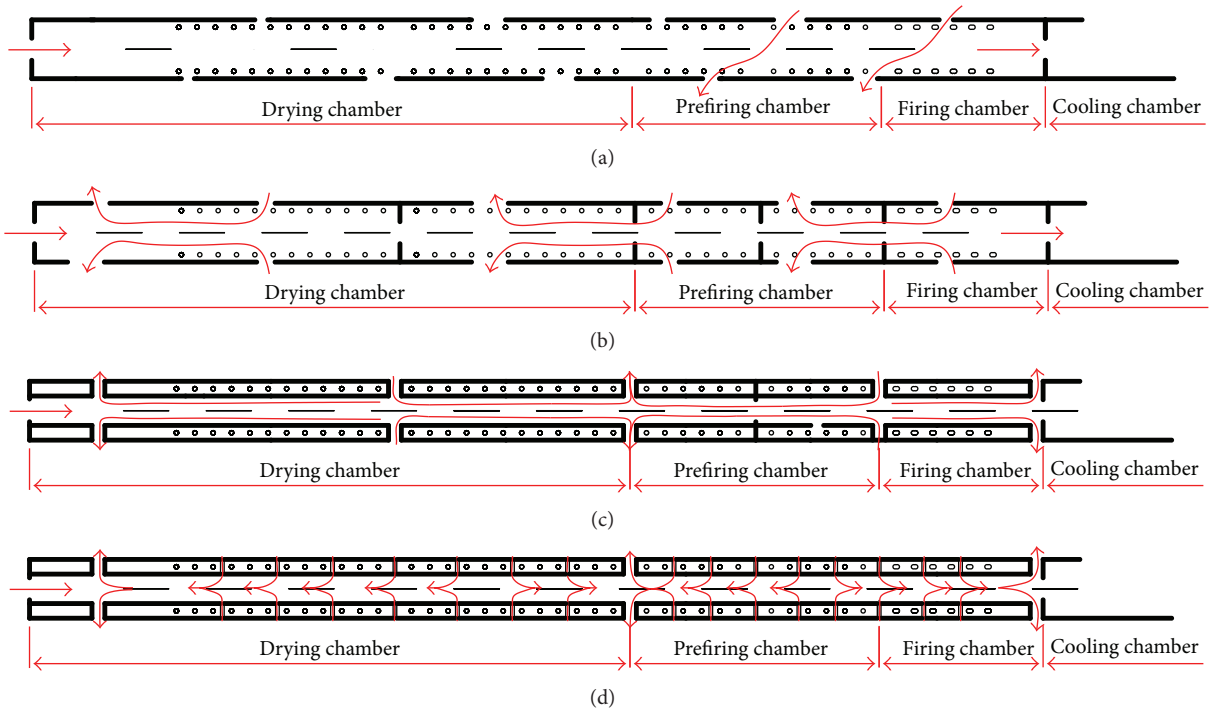

Figure 5: The longitudinal section model of the firing furnace.

Wacher [8] found that the smallest chamber height could attain the best temperature uniformity. Therefore, we proposed that the lamps were enclosed by quartz glass, and two pairs of gas inlets and three pairs of gas outlets were installed in the middle and at the ends of the furnace, as shown in Figure 5(c). Furthermore, the chambers of the furnace were smooth and narrow, facilitating laminar flow formation and rapid VOC removal.

Figure 5(d) shows that the lamps were enclosed by quartz glass, the fifteen pairs of inlets were evenly distributed in the furnace, and the three pairs of outlets were installed in the middle and at the ends of the furnace. Here, the chambers of furnace were smooth and narrow, containing more inlets and fewer outlets. Forming laminar flows and quickly removing VOC were enabled.

The longitudinal sections of the furnace were drawn up using traditional engineering computer aided design (CAD) software, as shown in Figure 6. Then, these sections were meshed in the preprocessing software, the integrated computer engineering and manufacturing code for computational fluid dynamics (ICEMCFD) with unstructured grids and triangular elements [9]. Finally, the messed models were exported into FLUENT. FLUENT can use grids comprised of triangular or quadrilateral cells (or a combination of the two) in 2D, and tetrahedral, hexahedral, polyhedral, pyramid, or wedge cells (or a combination of these) in 3D. So we choose the triangular cell of the mesh type to use in the simulation.

3.3. Parameter Setting. The options of pressure-based, transient, laminar, discrete ordinate (DO), dynamic mesh were selected; and the characteristic parameters of the silicon, quartz glass, and refractory were set in FLUENT. According to the firing process of the PV17, a paste produced by DuPont, the radiant powers of the lamps was set separately. The transport velocity of the solar cell was set to 0.1 m/sec, and the outlet pressure was set to negative 8 Pa. To speed up the calculation process, the initial temperature in the furnace was set to 150°C. The thermal conductivity of the solar cells is 148 W/m·K. The absorption coefficient of the solar cells is 10^5 m^{-1}. The specific heat of the solar cells is 700 J/kg·K. The density of the solar cells is 2329 kg/m^3.

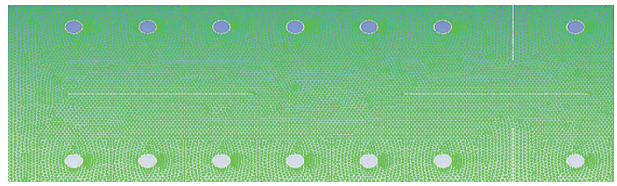

Figure 6: The longitudinal section model meshed in ICEMCFD.

The silicon wafers were stationary in RTP but in motion in the furnace. The movement affected the thermal field of the furnace; therefore, a dynamic mesh was used to study it, and the moving mesh boundary function was defined as follows:

$$((\text{move point } 2)\,(\text{time } 0\ 200)\,(v\_x\ 0.1\ 0.1)) \quad (14)$$

(see [10]), where move is the name of the function, point is the type of the function, 2 is number of points, v_x is the symbol of velocity in the x direction, and 0.1 is the velocity of the solar cells at 0 second and 200 seconds, whose unit is m/s.

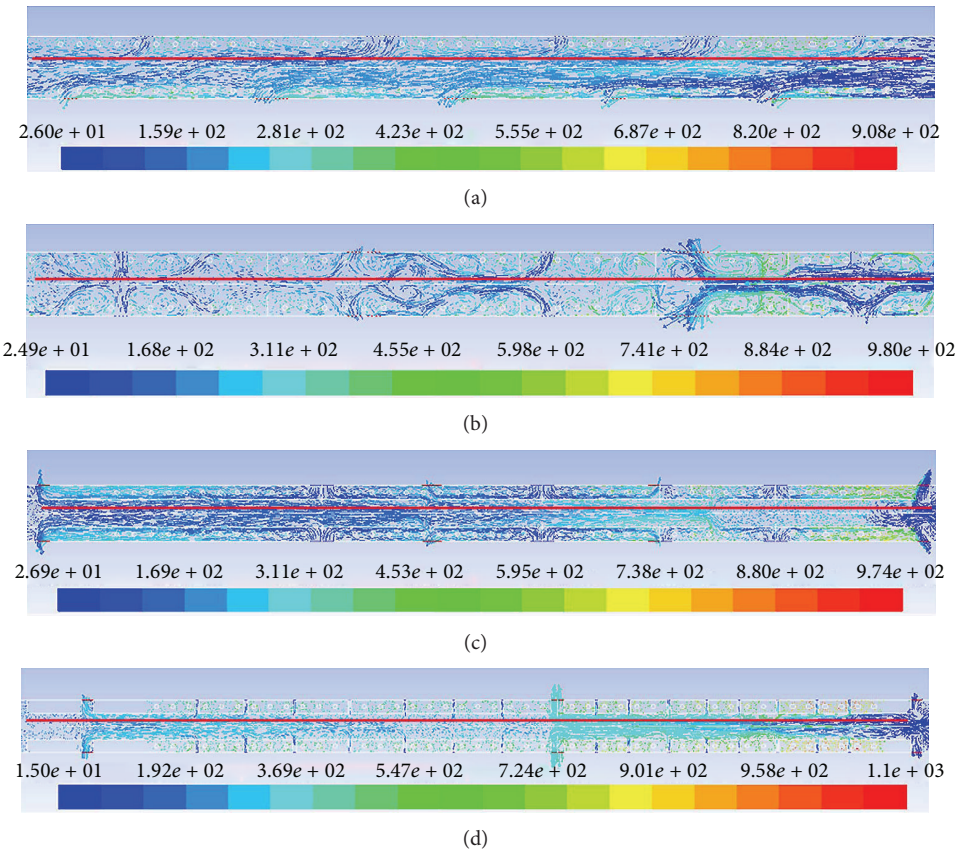

Figure 7: Velocity vectors and thermal distribution of the furnace for different settings of gas inlets and outlets.

3.4. Results and Analysis

3.4.1. Thermal Field Distribution. When the number of iterations increased, the transient thermal field gradually stabilized during the simulation, allowing the thermal distribution of the furnace to be obtained.

Figure 7(a) shows the thermal field distribution of Figure 5(a). The gas ran into the furnace from the upper inlets and drained out of the corresponding lower outlets in the direction opposite to the moving solar cells. However, the gas passed through the upper surface of one solar cell and the lower surface of another. Some metal ions evaporated from the upper surface of one solar cell to attach to the lower surface of another, causing contamination.

Figure 7(b) shows the thermal field distribution of Figure 5(b). The gas ran into the furnace from the upper and lower inlets in each chamber and drained out of the corresponding outlets in the opposite direction to the moving cells. Because it is divided into two layers, the gas flow was nonuniform; some of it surrounded the lamps, hindering VOC discharge.

Figure 7(c) shows the thermal field distribution of Figure 5(c). Due to the installment of quartz glass, the furnace chamber became narrow and smooth. The gas ran into the furnace from the upper and lower inlets and drained out of the corresponding outlets in the direction opposite to the moving cells. Because it is divided into two layers, the gas flow was uniform. However, there was a cutoff in the furnace chamber due to the decrease in the number of inlets, hindering VOC discharge.

Figure 7(d) shows the thermal field distribution of Figure 5(d). Due to the installation of the quartz glass, the furnace chamber became narrow and smooth. The gas ran into the furnace from the upper and lower inlets to drain out of the corresponding outlets in the direction opposite to the moving cells. The gas flow was divided into two uniform and continuous layers, meaning that the VOC discharged cleanly.

After comparing velocity vectors and thermal distribution of the furnace for different settings of gas inlets and outlets, the thermal field of Figure 7(d) is the most reasonable, making the structure of Figure 5(d) optimal.

3.4.2. Surface Temperatures of All Solar Cells. When the thermal field was stable, the solar cells were placed at the points of x-axis in the four models, respectively, and then the temperature of three points on each solar cell surface was obtained from the four simulation results simultaneously as shown in Figure 10. The average temperature of the solar cells' surface is the same as the firing curves of the PV17, a paste. Afterward, the temperature variance of each solar cell was calculated as shown in Figure 8. Curve-d was the lowest, meaning that its surface temperature was the most stable. Consequently, the structure of Figure 5(d) is optimal.

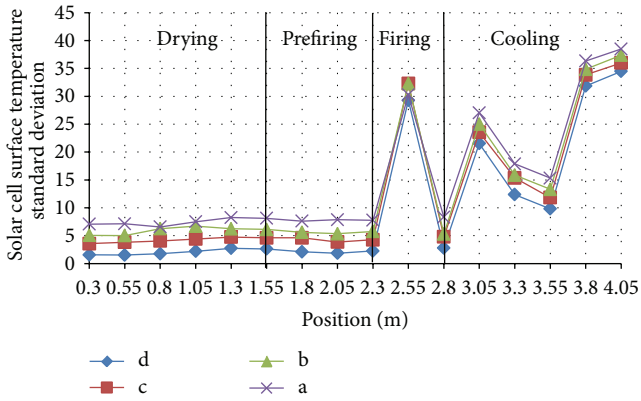

Figure 8: Temperature curves for the faces of the solar cells.

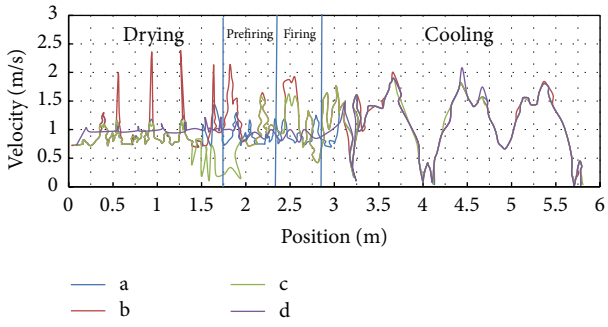

Figure 9: Airflow velocity vectors for the solar cell surface.

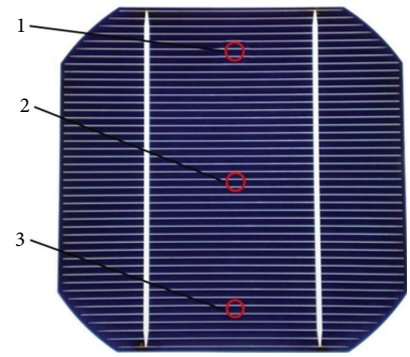

Figure 10: Solar cell.

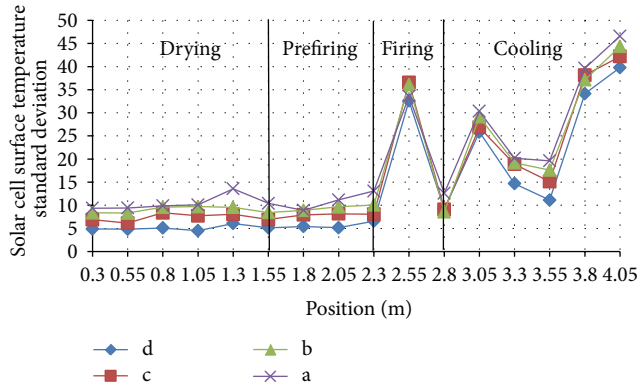

Figure 11: Temperature curves on the face of solar cells.

3.4.3. Gas Flow Velocities of Solar Cell Surface. When the thermal field was stable, the gas flow velocities 20 mm away from the upper surface of each solar cell in the furnace marked with red line in Figure 7 were extracted from the four simulation results simultaneously. Figure 9 shows that the fluctuation of curve-d was the least, meaning that the surface temperature was the most stable. Consequently, the structure of Figure 5(d) is optimal.

4. Model Verification

To verify the simulated result, solar cells that were fabricated on 125 × 125 mm^2, 2-Ω·cm resistivity, 200 μm thick, p-type, and Cz-Si wafers were textured using random pyramid formation. And the emitters were formed via $POCl_3$ diffusion. Furthermore, the wafers were coated with SiN_X via plasma enhanced chemical vapor deposition (PECVD). A front collection grid was created using screen-printed glass-fritted Ag paste. The Al paste was printed on the back with Ag/Al tabbing stripes [3].

4.1. Temperature Measurement of the Solar Cell. When the thermal field was stable, the solar cells were placed at the points of x-axis in the four models, respectively, and then a Q18 produced by Datapaq was used to measure the actual temperature of three points on each solar cell surface as shown in Figure 10 [2]. Figure 11 shows the surface temperature variations of each solar cell. Curve-d was the lowest, meaning that the temperature is the most uniform. Therefore, the structure of Figure 5(d) is the most reasonable. When comparing the curves in Figure 8, the actual temperature curves were almost the same as those obtained from the simulations.

4.2. Characteristic Measurement of Solar Cell. Four hundred pieces of solar material were made using this process. Afterward, they were divided into four groups and fired in the four experimental furnaces, respectively. Measured by IV-Measurement produced by Halm, Table 1 shows the average characteristic parameters for each group. The Eff (efficiency) and R_{sh} (shunt resistance) are minimized in Table 1-a. Furthermore, according to Figure 7(a), there may be metal contamination in Figure 5(a). The Eff and R_{sh} are maximized in Table 1-d. According to Figure 7(d), we think that the structure of Figure 5(d) is the most reasonable.

5. Conclusions

To investigate the influence of the gas flow on the thermal field of the furnace, the heat-transfer mechanism of the furnace was analyzed; four 2D physical models of the furnace and their corresponding numerical models were proposed.

Table 1: Solar cell characteristics.

	F.F. (%)	Eff. (%)	I_{sc} (A)	VOC (V)	R_s (Ω)	R_{sh} (Ω)
a	78.61	17.11	5.321	0.635	0.014312	800.213
b	79.23	17.23	5.361	0.642	0.011806	850.256
c	79.36	17.43	5.375	0.663	0.011612	1010.351
d	81.43	17.74	5.383	0.661	0.011003	1039.231

The following conclusions were obtained using these numerical simulations and experimental studies.

(1) The thermal field of the furnace was obtained using a simulation that included conduction, convection, and radiation.

(2) The temperature of a solar cell could be stable and uniform when the gas outlets were installed at the ends and in the middle of the furnace. Furthermore, the gas inlets were distributed evenly on the furnace.

(3) This work is useful for improving the efficiency of solar cells by optimizing the structure of solar cell manufacturing equipment.

2D models were used to simulate the thermal field of the furnaces, and effect of the mesh net on air flow was simplified, possibly generating differences relative to the practical thermal field in the study.

Conflict of Interests

The authors declare that there is no conflict of interests regarding the publication of this paper.

Acknowledgments

This work was supported by the National Natural Science Foundation (Contract no. 61176055) and a Grant from the Science and Technology Project (2011A080804009) of Guangdong Province, China.

References

[1] L. A. Dobrzański, M. Musztyfaga, A. Drygała, and P. Panek, "Investigation of the screen printed contacts of silicon solar cells using transmission line model," *Journal of Achievements in Materials and Manufacturing Engineering*, vol. 41, no. 1-2, pp. 57–65, 2010.

[2] J. Hoornstra, A. van der Heid, J. Bultman, and A. Weeber, "Simple, detailed & fast firing furnace temperature profiling for improved efficiency," in *Proceedings of the Conference PV in Europe—From PV Technology to Energy Solutions*, p. 276, 2002.

[3] I. B. Cooper, A. Ebong, J. S. Renshaw, R. Reedy, M. Al-Jassim, and A. Rohatgi, "Understanding and use of IR belt furnace for rapid thermal firing of screen-printed contacts to Si solar cells," *IEEE Electron Device Letters*, vol. 31, no. 5, pp. 461–463, 2010.

[4] S. A. Campbell, K.-H. Ahn, K. L. Knutson, B. Y. H. Liu, and J. D. Leighton, "Steady-state thermal uniformity and gas flow patterns in a rapid thermal processing chamber," *IEEE Transactions on Semiconductor Manufacturing*, vol. 4, no. 1, pp. 14–20, 1991.

[5] R. Kakoschke, E. Bußmann, and H. Föll, "Modelling of wafer heating during rapid thermal processing," *Applied Physics A*, vol. 50, no. 2, pp. 141–150, 1990.

[6] R. S. Gyurcsik, T. J. Riley, and F. Y. Sorrell, "A model for rapid thermal processing: achieving uniformity through lamp control," *IEEE Transactions on Semiconductor Manufacturing*, vol. 4, no. 1, pp. 9–13, 1991.

[7] ANSYS, Inc., *Fluent 12 Theory Guide*, 2009.

[8] A. Wacher and B. R. Seymour, "A radiation model of a rapid thermal processing system," *Mathematics in Industry Case Studies Journal*, vol. 3, pp. 1–18, 2011.

[9] ANSYS, Inc., *ICEM 12 Users Guide*, 2009.

[10] ANSYS, Inc., *Fluent 6.3 User's Guide*, 2006.